EES Catalysis

REVIEW ARTICLE

View Article Online
View Journal | View Issue

Cite this: *EES Catal.*, 2024, 2, 94

Research progress and perspectives on photocatalysts based on the lead-free double halide perovskite

Do Yeon Heo, Mahider Asmare Tekalgne and Soo Young Kim *

Photocatalytic technology stands as a promising solution to address the current energy and environmental challenges. Halide perovskites, particularly lead-free double halide perovskites, have garnered recognition as next-generation photocatalysts due to their adjustable bandgap, low binding energy, broad visible light absorption range, and efficient charge carrier transfer. In this review, we explore the utilization of lead-free double halide perovskites characterized by their non-toxic attributes and diverse chemical compositions and properties as photocatalysts for both hydrogen production and carbon dioxide reduction. We commence by presenting an overview of lead-free double halide perovskites, followed by a comprehensive analysis of recent research outcomes pertaining to their application as photocatalysts for hydrogen production and carbon dioxide reduction. Lastly, we discuss the challenges and prospects associated with lead-free double halide perovskite photocatalysts. This review is anticipated to serve as a valuable reference for the development of lead-free double halide perovskite-based photocatalysts, addressing critical aspects in the pursuit of achieving high-efficiency hydrogen generation and carbon dioxide reduction, crucial for our future energy and environmental needs.

Received 19th September 2023,
Accepted 23rd October 2023

DOI: 10.1039/d3ey00229b

rsc.li/eescatalysis

Broader context

In the ever-pressing quest for sustainable energy solutions and environmentally conscious technologies, photocatalytic advancements play a pivotal role. This review paper sheds light on a compelling avenue of research that showcases lead-free double halide perovskites as catalysts of substantial promise. Their ability to fine-tune bandgaps, their low binding energy, broad light absorption range, and effective charge transfer properties make them a new beacon in the realm of energy and environmental catalysis. The investigations discussed herein not only expand our comprehension of semiconductor materials but also hold immense potential for real-world applications. In particular, their application in the simultaneous production of hydrogen and the reduction of carbon dioxide marks a significant step towards sustainable energy solutions and mitigation of climate change. This work exemplifies the impact of materials science on critical energy and environmental challenges and paves the way for greener, more efficient future technologies. The findings underscore the importance of innovative, non-toxic materials in addressing our contemporary global challenges and herald a promising era for energy and environmental catalysis.

1. Introduction

The Earth's temperature has increased by more than 1.2 °C compared to pre-industrial levels. If current trends persist, the Paris Agreement's target of limiting global warming to 1.5 °C is expected to be reached by 2035.[1] The primary driver of global warming is the presence of greenhouse gases, which traps infrared radiation while allowing visible light to pass through. This imbalance in energy absorption and emission results in a net increase in Earth's temperature, leading to a range of severe consequences, including floods, heatwaves, cold spells, reduced solar reflectance, and rising sea temperatures.

Among greenhouse gases, carbon dioxide (CO_2) emissions from fossil fuels, the predominant source of energy, account for a staggering 76% of the total volume. Consequently, there is an urgent need to reduce greenhouse gas concentrations and develop sustainable energy technologies as viable alternatives. Solar energy, as the most abundant renewable energy source, holds immense promise. Harnessing the solar energy incident on Earth for various applications is crucial, with the potential to meet global energy demands within a relatively short timeframe. While solar energy technologies have primarily focused on electricity generation, a novel approach exists, leveraging solar energy to drive or initiate chemical reactions—a field known as photocatalysis. Photocatalysis finds applications in diverse areas, including hydrogen (H_2) production, CO_2 conversion, and pollution abatement, offering

Department of Materials Science and Engineering Korea University, Seoul 02841, Republic of Korea. E-mail: sooyoungkim@korea.ac.kr

significant potential to address our current energy and environmental crises.[2]

The concept of photocatalysis was first introduced by Fujishima and Honda in 1972, utilizing titanium dioxide as a photocatalyst to demonstrate hydrogen production through solar-driven water splitting.[3] This groundbreaking discovery sparked extensive research into solar energy conversion using photocatalysts. Numerous materials have been explored for photocatalysis, encompassing metal oxides,[4–8] metal nitrides,[9,10] metal sulfides,[11–13] metal–organic frameworks,[14–17] covalent organic frameworks,[18,19] and metal halides.[20] However, many of these materials present limitations such as inefficient utilization of visible light, rapid recombination of charge carriers, and instability. Additionally, some photocatalyst components may not align with environmental sustainability goals.[21,22] Nonetheless, halide perovskites have exhibited remarkable photocatalytic performance owing to their strong response to visible light, prolonged charge carrier lifetimes, high light absorption coefficients, and minimal non-radiative carrier recombination.[23] Although lead-based perovskites were initially employed as photocatalysts,[24] their commercial viability is hampered by their solubility in water, resulting in the release of toxic lead. Consequently, the development of lead-free halide perovskite materials has emerged as a critical objective.

Lead-free halide perovskites have garnered considerable attention across a range of fields, including perovskite solar cells,[25–29] light-emitting diodes,[30–33] X-ray detectors,[34,35] memristors,[36,37] and more. The substitution of lead with alkali metals in halide perovskites leads to an increase in the electronic bandgap,[38,39] which significantly influences photocatalytic performance. For efficient solar energy utilization, extending light absorption into the visible spectrum is essential, necessitating a photocatalyst with a bandgap energy less than 3 eV.[40] Moreover, semiconductor photocatalysts designed for water splitting require a minimum bandgap of 1.23 eV, and research has demonstrated that photocatalysts with bandgaps exceeding 2 eV exhibit superior performance.[41] Double perovskites, characterized by their diverse chemical compositions and properties relative to traditional perovskite structures, offer tunable bandgaps that can enable effective photocatalytic properties.

In this review, we aim to provide insights into recent research and future prospects of lead-free double perovskites as photocatalysts in environmentally sustainable industries, with a specific focus on H_2 production and CO_2 reduction. Our discussion will commence with an exploration of the theoretical foundations and synthesis methodologies associated with lead-free double perovskites and photocatalysts. Subsequently, we will introduce recent research endeavors pertaining to lead-free double perovskite photocatalysts in the context of H_2 production and CO_2 reduction, culminating in a discussion of the challenges and prospects shaping the future of this dynamic field.

2. Double halide perovskite

2.1. Crystal structure

The traditional crystal structure of perovskites adopts a cubic structure denoted as ABX_3. In contrast, double perovskites share similarities with the conventional perovskite structure but are composed of trivalent cations (B^{3+}) and monovalent cations (B^{+}) instead of the typical divalent cation (B^{2+}), as shown in Table 1. The chemical formula for double perovskite is represented as $A_2B^{+}B^{3+}X_6$. The structure of double perovskites forms a cubic lattice. Within the A site, there are two different cations, while the B site contains two distinct anions. This arrangement results in alternating cations and anions at the corners of the cubes. In Fig. 1, it can be observed that A^{+} ions are coordinated with 12 X^{-} ions, whereas B^{+} and B^{3+} ions are coordinated with 6 X^{-} ions, forming a network structure known as rock-salt ordering.[42,43] Consequently, the unit cell can be understood as a doubled cubic perovskite, essentially a double perovskite structure.[41,44]

Table 1 Cation and anion composition in double perovskites

A	$CH_3NH_3^{+}$, $CH(NH_2)_2^{+}$, Cs^{+} *etc.*
B^{2+}	Pb^{2+}, Sn^{2+} *etc.*
B^{3+}	Bi^{3+}, Sb^{3+}, In^{3+} *etc.*
B^{+}	Ag^{+}, Cu^{+}, Na^{+} *etc.*
X	I^{-}, Br^{-}, Cl^{-}

The structural stability of a double perovskite can be determined through the octahedral (μ) and Goldschmidt (t) tolerance factors. μ evaluates the stability of BX_6 octahedra, while t indicates the degree of distortion in the perovskite structure. These factors can be calculated using the following formulas:[45]

$$\mu = \frac{r_B}{r_X}$$

$$t = \frac{(r_A + r_X)}{\sqrt{2}(r_B + r_X)}$$

Here, r_A, r_B, and r_X represent the radii of the respective ions in the material. Both t and μ can be adjusted by substituting ions with different-sized elements. For perovskites to form a stable structure, it is generally accepted that $0.75 < t < 1$ and $\mu > 0.41$. Particularly, cubic structures within the range $0.9 \leq t \leq 1.0$ are

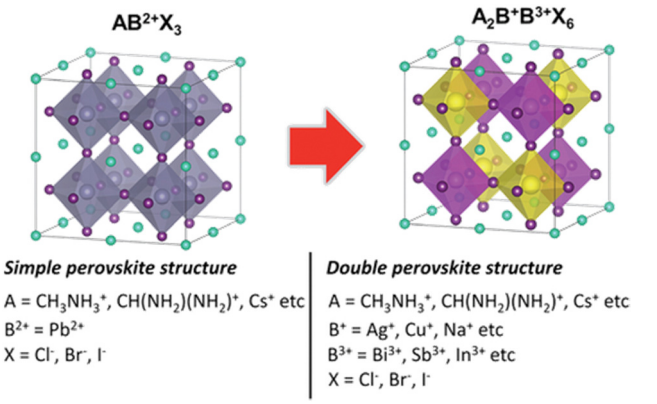

Fig. 1 Illustration of structural contrasts between simple ($AB^{2+}X_3$) and double perovskites ($A_2B^{+}B^{3+}X_6$). Visualization of A^{+}, B^{2+}, B^{+}, B^{3+}, and X^{-} ions depicted as cyan, gray, yellow, pink, and purple spheres, respectively.[43] Reproduced with permission from ref. 43 © 2019 Wiley-VCH Verlag GmbH & Co. KGaA, Weinheim.

considered the most stable perovskite structures. Furthermore, stable tetragonal structures can be achieved within the range $0.44 < \mu < 0.9$.[46] Thus, ion substitutions favoring the formation of cubic structures represent one of the best routes to realize stable perovskite structures. However, only specific metal ions that simultaneously satisfy both criteria can create such structures.

2.2. Synthesis protocol

2.2.1. Hot injection method. The hot injection method involves conducting chemical reactions or material synthesis at high temperatures. Because these reactions occur at elevated temperatures, molecular collisions and interactions between components become more vigorous. Consequently, reactions progress quickly, leading to a rapid synthesis rate. Often, this method involves a single step, simplifying the reaction process, which can save both time and cost. Additionally, by adjusting parameters like temperature and reaction time, one can finely control the properties of the resulting materials. Reactions at high temperatures can promote crystal growth, resulting in larger and more uniform crystal structures, thereby enhancing the optical and electrical properties of the materials. However, a drawback of the hot injection method is that it is not suitable for substances sensitive to heat.

The general steps of the hot injection method are as follows (see Fig. 2(a)):[47]

1. Mix reactants in the required proportions in a solvent, creating the reaction mixture to control the reaction environment and promote the reaction.

2. Place the synthesis reaction vessel into a heat conversion device and heat it to a high temperature.

3. Once the reaction is complete, cool and separate the components.

4. Harvest and refine the perovskite powder produced in the reaction vessel, removing any by-products or remaining residues to obtain pure perovskite.

By adjusting the elemental composition of the reactants, the type of ligand used, and the reaction temperature, one can modify the shape and size of the resulting nanoparticles. The hot injection method is a convenient way to produce nanoparticles with well-dispersed cubic $CsPbBr_3$ nanocubes, as demonstrated by Vighnesh *et al.*[47] They outlined a comprehensive hot injection protocol for synthesizing $CsPbBr_3$ nanocrystals, considering both intrinsic and extrinsic factors affecting

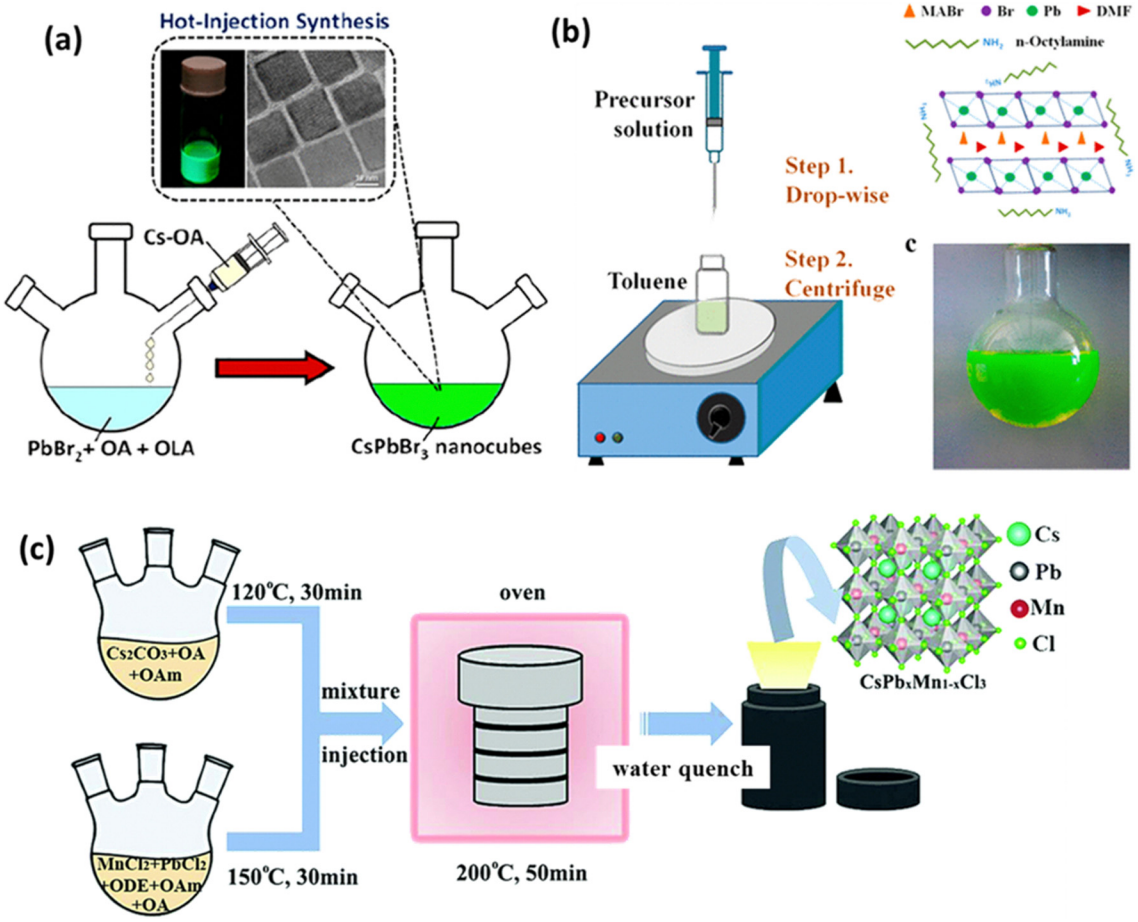

Fig. 2 Diagram depicting perovskite synthesis techniques: (a) hot injection,[47] (b) LARP,[50] and (c) solvothermal method.[53] Reproduced with permission from ref. 47 Copyright © 2022 American Chemistry Society. Reproduced with permission from ref. 50 Copyright © 2015 American Chemistry Society. Reproduced with permission from ref. 53 Copyright © 2018 Royal Society of Chemistry.

reproducibility. The protocol covered aspects such as precursor solution preparation, ligands, the roles of temperature and solvents, nanocrystal refinement, and storage. Moreover, the hot injection method has also been used for synthesizing double perovskites. $Cs_2Na_{1-x}Ag_xBiCl_6$ nanocrystals were synthesized through a hot injection method by reacting metal carboxylates and carbonates with benzoyl chloride to induce nucleation and growth.[48]

Liu *et al.* successfully synthesized $Cs_4CuIn_2Cl_{12}$ double perovskites using a moisture-assisted hot injection method, overcoming the challenges posed by moisture, which is known to be detrimental in nanocrystal synthesis.[49] They demonstrated that the presence of water molecules during $Cs_4CuIn_2Cl_{12}$ synthesis improves photoluminescence quantum yields, induces morphological transformations from 3D nanocubes to 2D nanoplatelets, and triggers photocarrier trapping. The hot injection method offers ease of modification in the synthesis process, making it a widely used approach in perovskite synthesis.

2.2.2. Ligand-assisted reprecipitation method. The ligand-assisted reprecipitation (LARP) method is employed for synthesizing nanoparticles with desired characteristics by controlling the size and shape of the nanoparticles using ligands. This method proves valuable for adjusting the color, optical properties, surface features, and more of the resulting nanoparticles. The process typically follows these general steps (see Fig. 2(b)):[50]

1. Prepare a precursor solution of perovskite by dissolving it in a solvent.

2. Dissolve ligand molecules in the solvent and add them to the precursor solution. Ligands play a crucial role in controlling the growth and morphology of nanoparticles.

3. Heat the ligand-treated solution in a reaction vessel using an appropriate heat source, initiating the formation of ligand-perovskite complexes.

4. Upon completion of the reaction, cool the solution to promote nanoparticle formation.

5. Separate and purify the formed perovskite nanoparticles. During this step, any by-products or remaining impurities are removed to obtain pure perovskite nanoparticles.

LARP allows for the synthesis of perovskite nanoparticles at room temperature without the need for high-temperature reactions. However, maintaining purity during synthesis can be challenging due to the rapid recrystallization rate associated with this method.

Yoo *et al.* investigated the impact of carboxylic acid and carboxylamine ligands on the size, shape, and crystal structure of $CsPbBr_3$ nanocrystals synthesized using LARP.[51] They found that changes in carboxylic acid length primarily affected the shape and crystal structure of the perovskite nanocrystals, while increasing the carboxylamine ligand length led to a decrease in nanoparticle size, with no significant impact on shape. Additionally, they demonstrated that carboxylic acid ligands directly bond to the perovskite nanocrystals, whereas carboxylamine ligands either directly or indirectly interact with the perovskite nanocrystals through amine ligands. LARP has also been used for synthesizing $Cs_2AgSbCl_6$ nanocrystals, which are employed as photocatalysts.[52] By controlling the surface ligand density through α-alkylation of aldehydes, high alkylation yields were achieved.

2.2.3. Solvothermal method. The solvothermal method involves synthesizing materials by subjecting them to high-temperature and high-pressure conditions in the presence of a solvent. The general steps of this process are as follows (see Fig. 2(c)):[53]

1. Dissolve metal precursors and halide compounds in an initial solvent. The reason for heating the initial reaction medium to temperatures exceeding 100 °C in the solvothermal method is to ensure the necessary reaction rate and thermodynamic stability for synthesizing complex compounds like double perovskites. At this stage, ligand molecules are added to facilitate interaction with metal precursors.

2. Use the solvent within a reactor to create high-temperature and high-pressure conditions, initiating chemical reactions leading to the formation of perovskite nanoparticles. Ligands can influence the size and shape of nanoparticles during this process.

3. Upon completion of the reaction, cool the mixture, promoting nanoparticle formation.

4. Separate and refine the formed perovskite nanoparticles.

Solvothermal reactions offer control over the resulting product's characteristics based on reactor design, parameter settings, and the choice of ligands. Ligands play a crucial role in adjusting nanoparticle size, shape, dispersion, and other properties. Compared to the hot injection method, which can be challenging for heat-sensitive materials, the solvothermal method allows for chemical reactions at high temperatures and pressures using solvents, making it suitable for a wide range of material syntheses. Chen *et al.* synthesized Mn-doped $CsPbCl_3$ using both the hot injection and solvothermal methods, demonstrating that the nanocrystals produced by the solvothermal method exhibited better stability.[54] They explained that the solvothermal method can provide more energy due to its operation at high temperature and pressure, enhancing the binding of Mn^{2+} within the ligand field of $CsPbCl_3$.

As an application of the solvothermal method, there is the microwave-assisted solvothermal method. This technique employs microwave energy to synthesize nanoparticles under high-temperature and high-pressure conditions. Microwave energy is delivered in the form of electromagnetic waves and rapidly transfers heat throughout the material, significantly increasing reaction rates and allowing for the synthesis of smaller nanoparticles. $Cs_2AgBiBr_6$ nanocrystals were synthesized using the microwave-assisted solvothermal method in combination with the solvent IPA (isopropanol), which efficiently absorbs microwave energy.[55] The $Cs_2AgBiBr_6$ nanoparticles synthesized by Slavney *et al.* in a simple and fast (2 min synthesis) method had a long carrier lifetime of 921 ns, comparable to the single crystal form (668 ns).[56]

2.3. Lead-free double halide perovskite (LFDHP) and their stability

Perovskites with the $APbX_3$ structure have been extensively researched due to their high efficiency in various applications such as photovoltaics and LEDs. However, the use of Pb

compounds has been globally restricted or prohibited since the 2000s due to the risk of lead poisoning upon human exposure.

Therefore, research on lead-free perovskites is essential for the commercialization of perovskite applications. Substituting Pb^{2+} with 2+ cations like Sn^{2+} and Ge^{2+} was attempted, but these alternatives suffer from instability issues due to their unstable oxidation states.[57–59] Consequently, research turned to partial doping of lead, although this approach does not provide a fundamental solution to lead toxicity.[60–62] Thus, there is an urgent need to explore new materials to address toxicity and stability issues, with lead-free double halide perovskites emerging as a potential solution.

As previously mentioned, stable perovskites are formed when $0.9 \leq t \leq 1.0$ and $0.44 < \mu < 0.9$. To assess the thermodynamic stability of $A_2B^+B^{3+}X_6$ double perovskites, the decomposition energy for possible decomposition pathways is calculated. Typically, halide perovskites are synthesized through reverse reactions, and the decomposition enthalpy can be calculated using the following equation:[63]

$$\Delta H = 2E[\mathrm{AX}] + E[\mathrm{B^+X}] + E\left[\mathrm{B^{3+}X_3}\right] - E\left[\mathrm{A_2B^+B^{3+}X_6}\right]$$

If ΔH is positive, the double perovskite is considered thermodynamically stable. According to Zhao *et al.*, most $A_2B^+B^{3+}X_6$ compounds exhibit significantly large positive values of ΔH, indicating excellent thermodynamic stability.[63] Exceptionally, materials containing iodides and Au have small or negative ΔH values, and the trend shows decreasing ΔH values from fluorides, chlorides, and bromides to iodides. Additionally, Cs_2AuBiF_6 and Cs_2KSbI_6 were found to have thermodynamically stable crystal structures despite having negative ΔH values. This discrepancy between crystallographic stability and thermodynamic stability is attributed to the complex ion mixing and covalent bonding nature of perovskites. Besides binary decomposition pathways, possible ternary compound-related decomposition pathways should also be considered. $Cs_2AgBiCl_6$, $Cs_2AgBiBr_6$, $Cs_2NaBiCl_6$, and Cs_2KBiCl_6 all demonstrate thermodynamic stability in both experimental and theoretical approaches.[64–68] Furthermore, among 64 candidates, researchers have identified 11 non-toxic $A_2B^+B^{3+}X_6$ perovskites that are suitable as light absorbers, taking into account properties such as decomposition enthalpy (ΔH), band gap, effective carrier masses (m_e^*, m_h^*), and exciton binding energy (ΔE_b), as summarized in Fig. 3(a).[63] Zhao *et al.* systematically compiled this data through first-principles calculations.

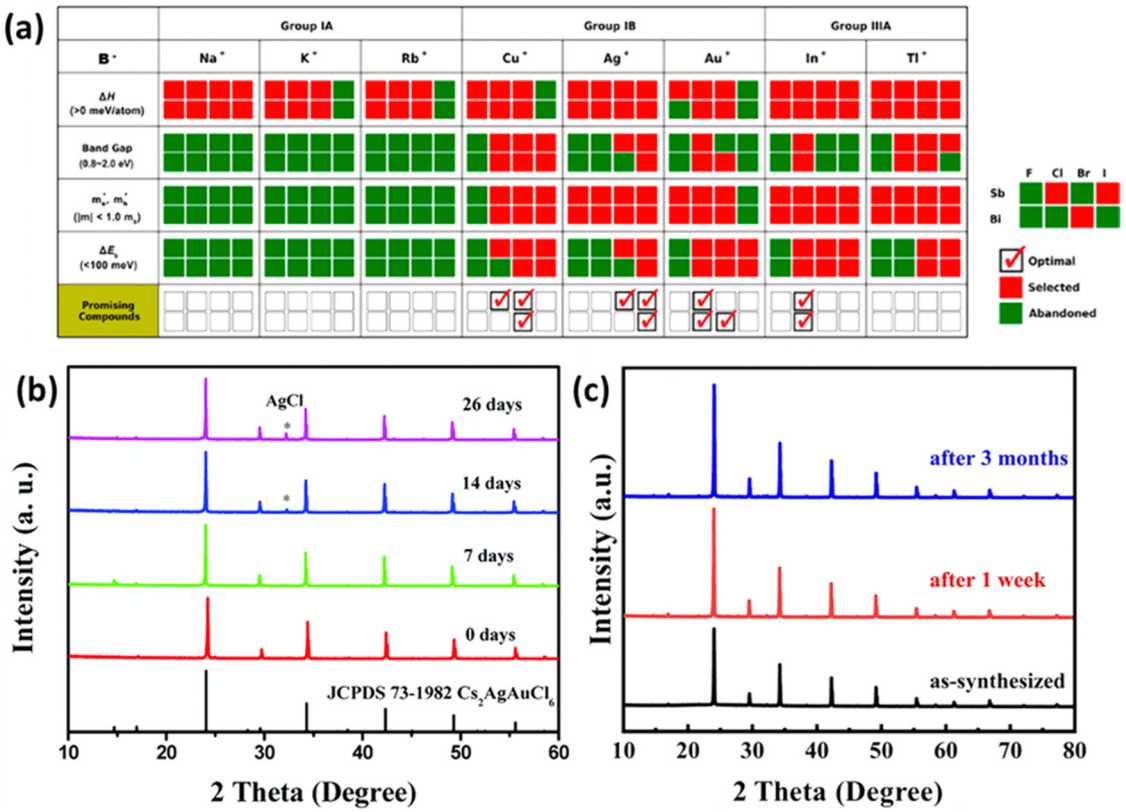

Fig. 3 (a) Stepwise materials evaluation process for photovoltaic performance, considering parameters such as decomposition enthalpy (ΔH), band gap, effective carrier masses (m_e^*, m_h^*),, and exciton binding energy (ΔE_b). Materials successfully passing the screening are indicated by red squares (Selected), while those not meeting the criteria are marked with green squares (Abandoned). The optimal environmentally friendly $A_2M^+M^{3+}X_6^{VII}$ perovskites meeting all criteria are denoted by red checkmarks.[63] Reproduced with permission from ref. 63 Copyright © 2017 American Chemistry Society. (b) XRD of $Cs_2AgInCl_6$ after 7 days, 14 days and 26 days of exposure to light and moisture conditions.[72] Reproduced with permission from ref. 72 Copyright © 2017 RSC. (c) XRD patterns of $Cs_2InAgCl_6$ after storage for one week and three months under ambient conditions.[73] Reproduced with permission from ref. 73 Copyright © 2021 Elsevier Inc. All rights reserved.

One persistent challenge with perovskites is their vulnerability to light and moisture. In particular, Methylammonium lead iodide ($MAPbI_3$) undergoes accelerated degradation to PbI_2 when exposed to light or moisture, resulting in a severe drop in performance.[69] In contrast, halide double perovskites have been shown to be stable under ambient conditions through extensive research. $Cs_2AgBiBr_6$, known for its high stability, has been investigated in various fields. Films of $Cs_2AgBiBr_6$ used in photodetectors maintained excellent intrinsic and environmental stability for up to two weeks.[70] These films exhibited stability in thermal tests within a temperature range of 20–120 °C and continuous ultraviolet irradiation tests. $Cs_2AgBiBr_6$ films designed for neuromorphic computing retained stable operation even after 20 days of storage in ambient conditions (approximately 40–50% humidity and around 25 °C).[71] X-ray diffraction (XRD) confirmed the maintenance of stable forms in $Cs_2AgInCl_6$ synthesized by Zhou even after 26 days of exposure to light and humidity as shown in Fig. 3(b).[72] Another study found that $Cs_2AgInCl_6$ remained stable in an air ambient environment for three months as shown in Fig. 3(c).[73]

Mechanical stability, which relates to a material's ability to restore its structure under applied distortion pressure, is also crucial. Many systems with the chemical structure of $A_2B^+B^{3+}X_6$ double perovskites are known to possess mechanical stability. Traditional mechanical stability for cubic phase crystals under equilibrium conditions requires satisfying the following elastic conditions:[74]

$$C_{11} - C_{12} > 0,\ C_{44} > 0,\ C_{11} + 2C_{12} > 0,\ C_{12} < B < C_{11}$$

$$B = \frac{C_{11} + 2C_{12}}{3}$$

$$G = \frac{1}{2}\left[\frac{C_{11} - C_{12} + 3C_{44}}{5} + \frac{5C_{44}(C_{11} - C_{12})}{4C_{44} + 3(C_{11} - C_{12})}\right]$$

Here, C_{11}, C_{12}, and C_{44} represent elastic constants, B represents bulk modulus, and G denotes shear modulus. Lower values of elastic constants indicate softer materials. Lower values of B and C_{11} imply weaker resistance to volume changes caused by applied pressure. $Cs_2AgFeCl_6$, for instance, exhibits low B values, indicating volume deformation under external stress.[75] Furthermore, the ratio of shear elastic modulus to bulk elastic modulus classifies Cs_2AgBiX_6 (X = Br, Cl) as ductile materials.[76]

3. Photocatalytic application

3.1. The principle of photocatalysts

As depicted in Fig. 4(a), visible and infrared light account for over 90% of the total solar energy.[77] To harness solar energy efficiently, the development of narrow bandgap photocatalysts is essential. In particular, the valence band maximum (VBM) position should be more positive than the potential of the oxidative half-reaction, while the conduction band minimum (CBM) position should be more negative than the potential of the reductive half-reaction. Due to the advantages of bandgap and band position adjustments, double-halide perovskites are considered promising candidates for photocatalysis. In semiconductor-based photocatalytic reactions, the role of the photocatalyst is to absorb light, generate photo-induced electron–hole pairs, and transport charge carriers to the surface to induce oxidative–reductive reactions. Photocatalysts typically have active sites on their surfaces to capture charges and activate reactants. The fundamental steps of a photocatalytic process can be seen in Fig. 4(b).[78]

(1) Photogenerated electrons jump from the valence band (VB) to the conduction band (CB) after accepting holes. This process occurs rapidly at the femtosecond level ($\sim 10^{-15}$ seconds).

(2 and 3) Subsequently, the electrons and holes migrate to the photocatalyst surface. Charge diffusion during this step is swift, occurring at the nanosecond level ($\sim 10^{-9}$ seconds).

(4 and 5) Electrons and holes approaching the surface are utilized by catalytic active sites to initiate the desired oxidative–reductive reactions. This is a relatively slow process occurring at the microsecond to millisecond range (10^{-6} to 10^{-3} seconds).

(6) Electron–hole pairs can recombine with each other, generating energy in the form of fluorescence or heat within nanoseconds.[78,79]

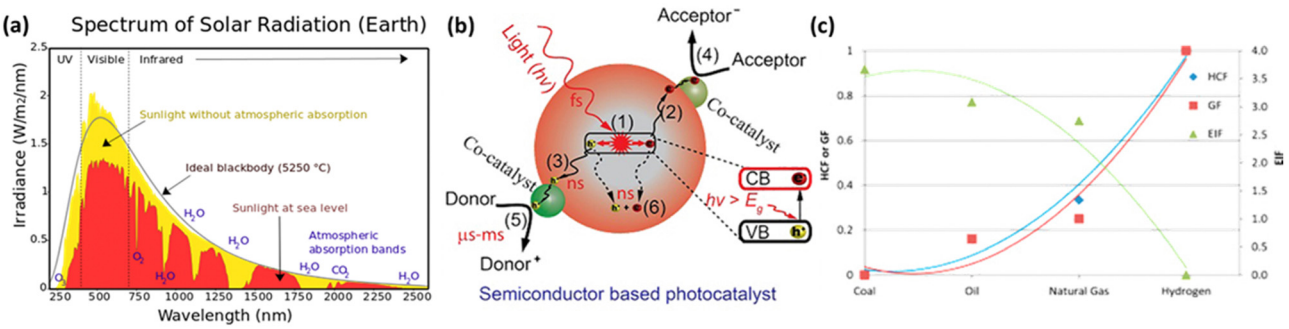

Fig. 4 (a) Illustration of the solar spectrum and absorption by atmospheric gases in the wavelength range of 240 nm to 2.5 μm.[77] Reproduced with permission from ref. 77 Copyright *via* Wikimedia Commons. (b) Fundamental operating mechanisms of semiconductor-based photocatalysts.[78] Reproduced with permission from ref. 78 Copyright © 2022 Tsinghua University Press Ltd. (c) Comparison of Hydrogen Combustion Efficiency (HCF), Greenhouse Gas Footprint (GF), and Energy Intensity Factor (EIF) between hydrogen and other fossil fuels.[81] Reproduced with permission from ref. 81 Copyright © 2014 Hydrogen Energy Publications, LLC. Published by Elsevier Ltd. All rights reserved.

3.2. Photocatalysis for H_2 production

Hydrogen is gaining attention as a promising renewable fuel source because it offers energy without carbon emissions. Unlike conventional electricity, hydrogen fuel can utilize storage and transportation infrastructure, and it can be stored for extended periods. Hydrogen can be stored as a gas, liquid, or absorbed in metal hydrides. Additionally, the production of hydrogen benefits from an abundant water supply, and there are no exhaust emissions during the production process. As shown in Fig. 4(c), as the hydrogen content factor (HCF) increases, the greenization factor (GF) rises, while the environmental impact factor (EIF) decreases.[80,81] EIF_{max} is considered for coal. In other words, hydrogen is expected to play a crucial role in reducing carbon emissions.

Hydrogen can be produced from various forms of energy sources, including electricity, heat, light, and biochemical processes. Among these, hydrogen production using photocatalysis converts photon energy into chemical energy (hydrogen). To choose the optimal photocatalyst for hydrogen production, the rapid generation and separation of electron–hole pairs are essential. Semiconductors and metal oxides have been extensively studied as photocatalysts. Semiconductors with narrower bandgaps can harvest more visible light, enabling them to utilize solar energy more effectively and achieve higher solar-hydrogen efficiency. However, the bandgap of semiconductors should theoretically be greater than 1.23 eV, and practical consideration of overpotential is required for actual oxidative–reductive reactions. Photoreduction and photooxidation reactions are expressed as follows:[80]

$$\text{Photoreduction:}\quad 2H_2O + 2e^- \xrightarrow{h\nu} H_2 + 2OH^-$$

$$\text{Photo-oxidation:}\quad 2H_2O \xrightarrow{h\nu} O_2 + 4H^+ + 4e^-$$

3.3. Photocatalysis for CO_2 reduction

Converting CO_2 into CO and hydrocarbons requires a substantial amount of energy. Therefore, photocatalytic CO_2 conversion using solar energy is a promising technology for reducing CO_2 emissions. While photocatalytic CO_2 reduction technology offers the advantage of reducing greenhouse gas concentrations and producing available energy sources, it faces the challenge of relatively low overall efficiency. The CO_2 conversion process unfolds as follows:[82]

1. CO_2 molecules adsorb onto the photocatalyst's surface.

2. The photocatalyst absorbs photons with energy greater than its bandgap, generating electron–hole pairs in the conduction and valence bands.

3. The photo-generated electrons and holes then move to the surface of the photocatalyst.

4. The electrons react with adsorbed CO_2 on the surface to produce CO and hydrocarbons.

5. Finally, the generated products (CO and hydrocarbons) are desorbed from the surface.

Through this conversion technology, both C_1 and C_{2+} products can be produced.[83] Notable C_1 products include CO, CH_4, HCOOH, and CH_3OH, while C_{2+} products include C_2H_4, C_2H_5OH, C_2H_6, propanol, and acetone. C_{2+} products have broader applications and higher added value compared to C_1 products. They boast high energy density and play a significant role in the chemical industry. Specifically, C_2H_4 is a primary component used in various plastic and cosmetic productions, while C_2H_5OH serves as alcohol beverages, pharmaceutical preservatives, and fuel. Given their higher value and derivation from C_1 products, proposing the production of C_{2+} through a single CO_2 reduction process is suggested.

Table 2 Reaction equations and corresponding standard redox potentials for CO_2 reduction to various products at pH = 7

Reaction equations	E_0 (V *vs.* NHE)	Main products
$CO_2 + 2H^+ + 2e^- \rightarrow HCOOH$	−0.61	Formic acid
$CO_2 + 2H^+ + 2e^- \rightarrow CO + 2H_2O$	−0.53	Carbon monoxide
$CO_2 + 4H^+ + 4e^- \rightarrow HCHO + H_2O$	−0.48	Formaldehyde
$CO_2 + 6H^+ + 6e^- \rightarrow CH_3OH + H_2O$	−0.38	Methanol
$CO_2 + 8H^+ + 8e^- \rightarrow CH_4 + 2H_2O$	−0.24	Methane
$2CO_2 + 8H^+ + 8e^- \rightarrow CH_3COOH + 2H_2O$	−0.31	Acetic acid
$2CO_2 + 14H^+ + 14e^- \rightarrow C_2H_6 + 4H_2O$	−0.51	Ethane

To enhance selectivity for C_{2+} products, it is essential to suppress the ratio of C_1 products and inhibit the hydrogen evolution reaction pathway. The preference for reaction pathways leading to desired products depends on the adsorption energies of intermediates at the active sites of the catalyst surface. Therefore, research on efficient photocatalysts for CO_2 conversion is required. Table 2 presents common chemical reaction equations and associated potentials for CO_2 reduction.[84] For instance, when converting CO_2 into CO, the photocatalyst's CBM and VBM should be less than −0.53 V and greater than +0.81 V, respectively. This implies that the photocatalyst's bandgap should be greater than 1.34 eV.

4. LFDHP photocatalytic for H_2 production

To utilize perovskite photocatalysts effectively, the bandgap needs to be reduced, and they should possess a broad absorption spectrum. Achieving this involves adopting 1+ and 3+ cations and arranging them orderly on the B-site to form double perovskites, as mentioned earlier. Let's delve into the research results on H_2 production using LFDHP photocatalysts.

4.1. Doping strategies for improved photocatalysis

Metal halide perovskites are ionic substances, making it challenging to use them directly as photocatalysts for water splitting. To overcome this issue, a concept called HX splitting was proposed, involving the use of saturated hydrohalic acid (HX) solutions. Saturated HX solution contributes to improving the activity of photocatalysts. HX splitting is employed by photocatalysts to absorb photon energy and facilitate chemical reactions, impacting charge transfer processes. Furthermore, it affects the chemical reactions occurring at the active sites on the surface of the photocatalyst, accelerating and enhancing

the efficiency of the reactions. In other words, the use of HX enhances the activity of the photocatalyst, leading to increased efficiency in chemical reactions. Li *et al.* combined Ag atoms with $Cs_3Br_2Br_9$ to induce the transformation into the double perovskite structure $Cs_2AgBiBr_6$.[85] They found that Ag atoms occupying vacancies eliminate the distortion of the $BiBr_6$ octahedra and remove strong localization of electron–hole pairs. As a result, $Cs_2AgBiBr_6$ exhibited lower exciton binding energy, higher carrier mobility, and longer lifetime, leading to a significant enhancement in photocatalytic performance (Fig. 5(a)). Additionally, when electron acceptor H_3PO_2 was introduced into HBr solution, the photocatalytic activity of $Cs_2AgBiBr_6$ was further improved, reaching 54.7 μmol g^{-1} h^{-1}, as seen in Fig. 5(b). This demonstrates that simple doping methods can enhance the photocatalytic properties of perovskites. Chen *et al.* synthesized $Cs_3Bi_{2x}Sb_{2-2x}I_9$ by doping Sb into $Cs_3Bi_2I_9$.[86] Sb doping effectively reduced the contribution of Bi^{3+} to the conduction band and mitigated the influence of Bi vacancies on the band structure (Fig. 5(c)). The introduction of Sb, with a smaller ionic radius than Bi, into $Cs_3Bi_2I_9$ has been found to reduce the contribution of Bi metal ions to the conduction band, thereby mitigating the impact of defects and decreasing the intermediate gap state. $Cs_3Bi_2I_9$ exhibited a photocatalytic activity of 1.12 μmol h^{-1} for HI solution, but after Sb doping, this activity significantly increased to 78.6 μmol h^{-1}, as shown in Fig. 5(d).

Surface defects in Bi-based materials have been reported to enhance surface charge separation and improve photocatalytic performance.[87,88] He *et al.* formed defect-rich $Cs_2AgBiBr_6$ by exposing $Cs_2AgBiBr_6$ to visible light, demonstrating that the formation of surface defects optimizes local atomic arrangements, electronic structures, and provides active sites for trapping electrons, leading to higher charge separation and increased photocatalytic efficiency.[89] The defect-rich $Cs_2AgBiBr_6$ exhibited powerful photocatalytic hydrogen evolution, reaching 4.06 μmol g^{-1} within 10 hours, about 5.27 times better than pristine $Cs_2AgBiBr_6$ (0.77 μmol g^{-1} within 10 hours), with sustained performance over 80 hours of photocatalytic reaction.

4.2. Composite strategies with 2D materials

Ongoing research aims to enhance the performance of LFDHP by combining them with 2D conductive materials. Reduced graphene oxide (RGO) is known for its excellent electron transfer properties and chemical stability. Wang *et al.* produced $Cs_2AgBiBr_6$/RGO composites through photoreduction and confirmed their photocatalytic activity.[90] Photogenerated electrons in $Cs_2AgBiBr_6$ migrate to the conductive RGO, where they reduce

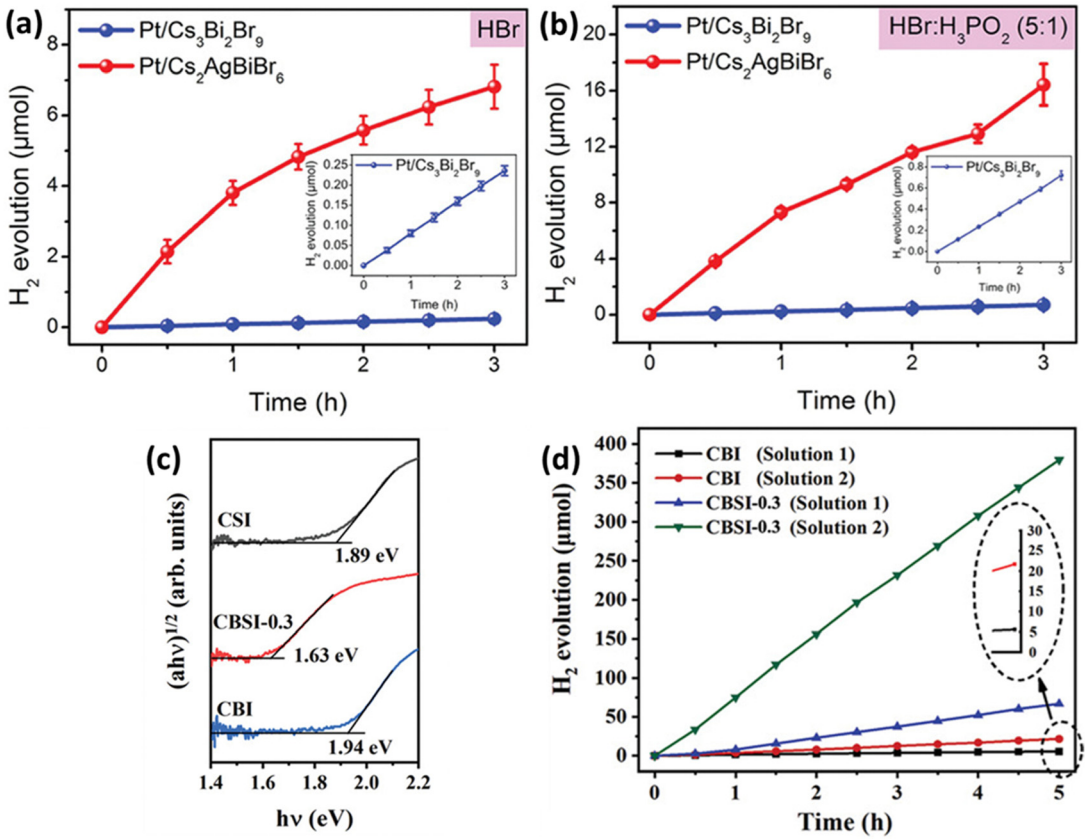

Fig. 5 Hydrogen evolution performance of $Pt/Cs_3Bi_2Br_9$ and $Pt/Cs_2AgBiBr_6$ in aqueous solutions of (a) HBr and (b) HBr/H_3PO_2.[85] Reproduced with permission from ref. 85 Copyright © 2020 Wiley-VCH Verlag GmbH & Co. KGaA, Weinheim. (c) Optical absorption spectra of $Cs_3Bi_2I_9$ (CBI), $Cs_3Sb_2I_9$ (CSI), and $Cs_3Bi_{2x}Sb_{2-2x}I_9$ (CBSI-0.3). (d) Comparative analysis of the hydrogen evolution activity between CBI and CBSI-0.3 in Solution 1 and 2.[86] Reproduced with permission from ref. 86 Copyright © 2020 Wiley-VCH GmbH.

H^+ to form H_2, while holes oxidize Br^- to Br_3^- on $Cs_2AgBiBr_6$ particles. The introduction of RGO significantly increased the H_2 production rate to ~80 times that of $Cs_2AgBiBr_6$ in HBr/H_3PO_2 solution and maintained high activity continuously for 120 hours. Another approach involves introducing nitrogen-doped carbon (N–C) into LFDHP to enhance charge transfer.[91] $Cs_2AgBiBr_6$/N–C demonstrated a high hydrogen evolution rate of 380 μmol g^{-1} h^{-1} under visible light irradiation ($\lambda \geq 420$ nm), which was 19 times higher than pure $Cs_2AgBiBr_6$ (Fig. 6(a)). High-surface-area N–C prevents perovskite aggregation and provides more pathways for the movement of photogenerated carriers. Nitrogen defects promote photogenerated electron transfer, spatially separating electrons and holes within perovskites, significantly improving photocatalytic performance.

Research also explores the use of LFDHP combined with transition metal dichalcogenides (TMDs) to achieve high hydrogen production rates and long-term stability. TMDs, such as MoS_2, have been widely used as photocatalysts for hydrogen evolution reactions (HER) due to their similar hydrogen binding energy to noble metal catalysts and excellent stability in HBr solutions.[92] Zhang *et al.* proposed a $MoS_2/Cs_2AgBiBr_6$ (MoS_2/CABB) composite photocatalyst that exhibited an HER rate of 87.5 μmol h^{-1} g^{-1}, which was about 20 times higher than $Cs_2AgBiBr_6$ (CABB) and even outperformed Pt/$Cs_2AgBiBr_6$ (Pt/CABB) as shown in Fig. 6(b).[93] The composite maintained excellent photocatalytic stability during a discontinuous 500 hour test over 40 days.

Auxiliary catalysts are used to facilitate electron transfer and electron–hole pair separation. Transition metal phosphides (TMPs) are gaining attention as alternative catalysts that can replace noble metals. Huang *et al.* synthesized the NiCoP/$Cs_2AgBiBr_6$ (NCP/CABB) composite through electrostatic binding.[94] The optimized NCP/CABB composite achieved a high H_2 generation rate of 373.16 μmol g^{-1} h^{-1}, which was about 88 times higher than pure CABB (4.23 μmol g^{-1} h^{-1}) and significantly superior to CABB/5% Pt (7.78 μmol g^{-1} h^{-1}). As shown in Fig. 6(c), the mechanism involves easy activation of electrons and holes under visible light, where electrons transfer easily from CABB's valence band to NCP's conduction band, facilitating the H_2 production reaction. The change in interfacial energy positions during electron transfer resulted in band bending at the interface. The introduction of highly conductive TMP nanoparticles enhanced photogenerated charge separation and movement, significantly improving photocatalyst performance.

4.3. Heterojunction approaches for enhanced photocatalysis

Recent research has revealed that a step-scheme (S-scheme) heterojunction composed of n-type reduction photocatalysts and n-type oxidation photocatalysts with staggered band alignment has a strong oxidation–reduction potential.[95–97] $Cs_2AgBiBr_6$ rich in Br-vacancies combined with WO_3 nanorods in an S-scheme heterojunction exhibited excellent photocatalytic properties.[98] Abundant Br-vacancies provided effective active sites, while the S-scheme heterojunction ensured efficient

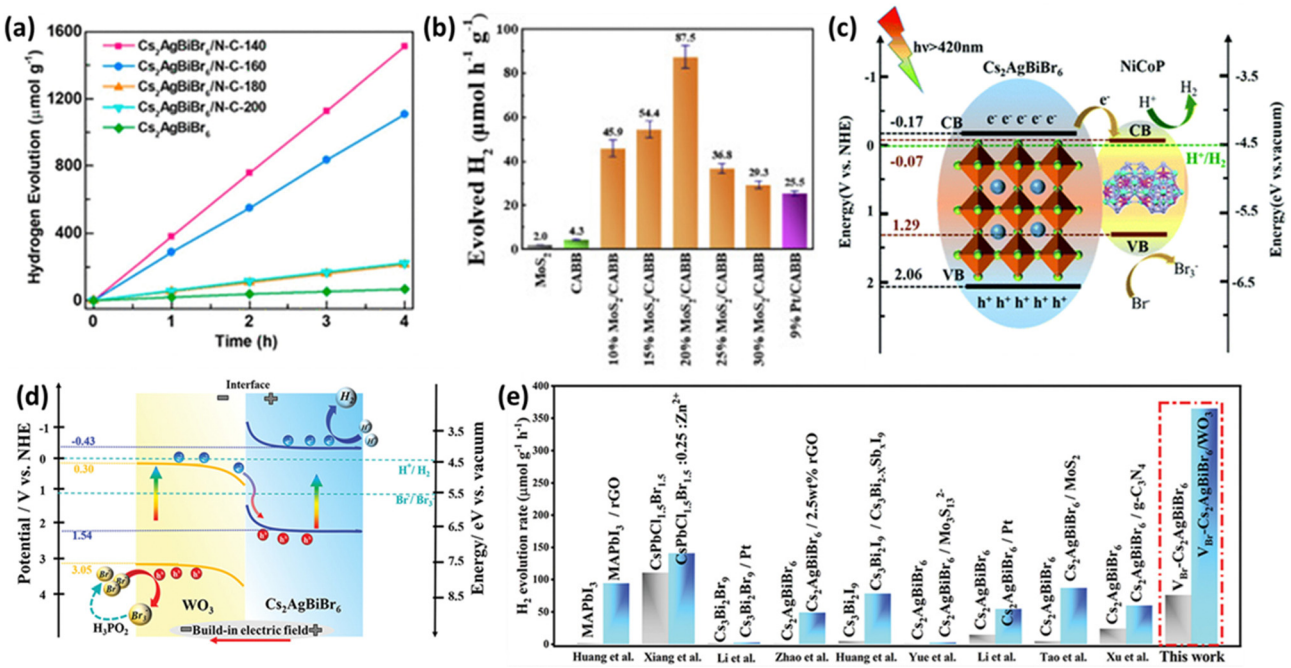

Fig. 6 (a) Hydrogen production rate from HBr aqueous solution using $Cs_2AgBiBr_6$ and $Cs_2AgBiBr_6$/N–C–Th composites under visible light with a cutoff filter ($\lambda \geq 420$ nm), and stability assessment.[91] Reproduced with permission from ref. 91 Copyright © 2021, American Chemistry Society. (b) Photocatalytic hydrogen evolution rates for MoS_2, CABB, MoS_2/CABB, and Pt/CABB under visible light illumination (300 mW cm^{-2}, $\lambda \geq 420$ nm).[93] Reproduced with permission from ref. 93 Copyright © 2021, American Chemical Society. (c) Mechanism for photocatalytic hydrogen generation over NiCoP (NCP)/$Cs_2AgBiBr_6$ (CABB).[94] Reproduced with permission from ref. 94 Copyright © 2022 Royal Society of Chemistry. (d) Schematic representation of charge transfer and dynamic equilibrium processes. (e) Comparative analysis of hydrogen evolution performance between previously reported perovskite-based catalysts and VBr-$Cs_2AgBiBr_6/WO_3$.[98] Reproduced with permission from ref. 98 Copyright © 2023 Wiley-VCH GmbH.

charge transfer at the interface (Fig. 6(d)). The optimized V_{Br}-$Cs_2AgBiBr_6/WO_3$ S-scheme photocatalyst demonstrated a high hydrogen evolution rate of 364.89 μmol g^{-1} h^{-1}, surpassing other perovskite-based catalysts (Fig. 6(e)). These findings highlight the promising potential of perovskite photocatalysts, especially LFDHP, in various applications with enhanced performance through doping, defect engineering, and composite strategies.

5. LFDHP photocatalytic for CO_2 reduction

In this section, we delve into the promising applications of LFDHP as photocatalysts for converting CO_2 into CO and hydrocarbons, highlighting their potential in addressing environmental challenges and clean energy generation.

5.1. LFDHP as photocatalysts

Zhou *et al.* synthesized $Cs_2AgBiBr_6$ nanocrystals using a simple hot injection method in Fig. 7(a) and used them as catalysts for CO_2 reduction.[99] They achieved a total electron consumption of 105 μmol g^{-1} under AM 1.5G illumination, demonstrating its significant potential as a photocatalyst (Fig. 7(b)). It also exhibited excellent stability in nonpolar solvents, 55% relative humidity, and thermal and light stability tests. Additionally, the performance of LFDHP photocatalysts was found to vary significantly depending on their morphology. Cs_2AgBiX_6 synthesized in a 2D nanoplatelet form outperformed nanocubes in CO_2 reduction, attributed to enhanced charge transport and longer diffusion lengths within nanoplatelets.[100]

Reducing the size of a material leads to an increase in its surface area. This, in turn, creates more active sites and shortens the distance for charges (electrons and holes) to move across the surface. As a result, the likelihood of electrons and holes recombining decreases.[101] This phenomenon enhances the activity of the photocatalyst. Pi *et al.* introduced the 3D hierarchical $Cs_2NaBiCl_6$ photocatalyst with abundant chlorine vacancies.[102] Fig. 7(c) depicts numerous 3D hierarchical microspheres assembled from nano flakes. Chlorine vacancies suppressed electron–hole recombination, enhanced CO_2 adsorption, and reduced the reaction energy barrier for CO_2 to CO conversion. This defect-engineered perovskite photocatalyst demonstrated a substantial electron consumption of 412.26 μmol g^{-1} during a 6 hour test.

5.2. Combining LFDHP with other materials

Combining LFDHP with other materials can enhance CO_2 reduction performance. Chen *et al.* synthesized $Cs_2AgInCl_6$ quantum dots *via* a hot injection method and controlled the Cl source to create composites with varying Ag loadings.[103] These composites exhibited improved CO_2 reduction efficiency through the surface plasmon resonance effect of Ag nanoparticles, achieving maximum yields of 26.4 μmol g^{-1} for CO and 28.9 μmol g^{-1} for CH_4 during CO_2 reduction. Furthermore, the study explored the CO_2 reduction capabilities of a 2D $Cs_2AgBiBr_6$ nanoflake-Cu-RGO heterostructure without organic

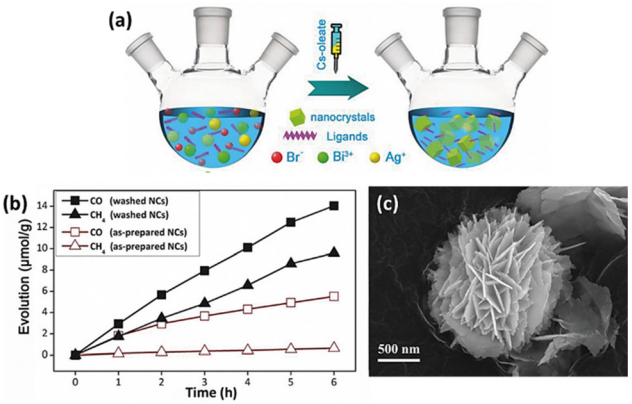

Fig. 7 (a) Diagram depicting the solution-phase synthesis of $Cs_2AgBiBr_6$ NCs using the hot-injection route. (b) Evolution of CO and CH_4 over as-prepared and washed $Cs_2AgBiBr_6$ NCs over time.[99] Reproduced with permission from ref. 99 Copyright © 2018 Wiley-VCH Verlag GmbH & Co. KGaA, Weinheim. (c) FE-SEM (Field Emission Scanning Electron Microscopy) image of $Cs_2NaBiCl_6$.[102] Reproduced with permission from ref. 102 Copyright © 2022 Wiley-VCH GmbH.

solvents, utilizing H_2O vapor as a proton source.[104] The results showed an overall enhancement in photocatalytic performance, particularly in CH_4 selectivity as shown in Fig. 8(a) and (b).

In a prior study, a 2D Bismuth monolayer exhibited a remarkable electrocatalytic efficiency in producing formate ($HCOO^-$) during CO_2 reduction reactions.[105,106] Building upon this foundational research, Sena *et al.* assembled $Cs_2AgBiBr_6$ onto this bismuth monolayer, creating a composite material.[107] This composite photocatalyst significantly improved charge separation and reduced the rate of electron–hole recombination, thereby enhancing the production and selectivity of the eight-electron CH_4 pathway. The $Cs_2AgBiBr_6$/Bi monolayer composite displayed outstanding photocatalytic activity, with rates of 1.49(±0.16) μmol g^{-1} h^{-1} for CH_4, 0.67(±0.14) μmol g^{-1} h^{-1} for CO, and 0.75(±0.20) μmol g^{-1} h^{-1} for H_2, along with a CH_4 selectivity of 81(±1)% based on one solar electron standard.

Among 2D materials, MXenes, with the general chemical formula $M_{n+1}XnT_x$ (M = early transition metal, X = carbon and/or nitrogen, T_x = surface group), exhibit excellent conductivity, high electrical capacity, a high elastic modulus, and an adjustable bandgap.[108] However, 2D nanosheets with atomic thickness often have limited light absorption capabilities.[109] As shown in Fig. 8(c), Zhang *et al.* proposed a self-assembled heterostructure of $Cs_2AgBiBr_6$ nanocrystals on MXene nanosheets' surfaces through mutual electrostatic interactions.[110] These MXene nanosheets effectively facilitated the formation of free charge carriers in $Cs_2AgBiBr_6$ nanocrystals by reducing the exciton binding energy. Consequently, this resulted in a high photocurrent consumption rate of 50.6 μmol g^{-1} h^{-1} during the photocatalytic reduction of CO_2 (Fig. 8(d)).

5.3. Z-Scheme systems for enhanced photocatalysis

In the pursuit of developing efficient photocatalysts, researchers have introduced a concept known as Z-scheme heterojunctions. These Z-scheme systems offer the advantage of spatially

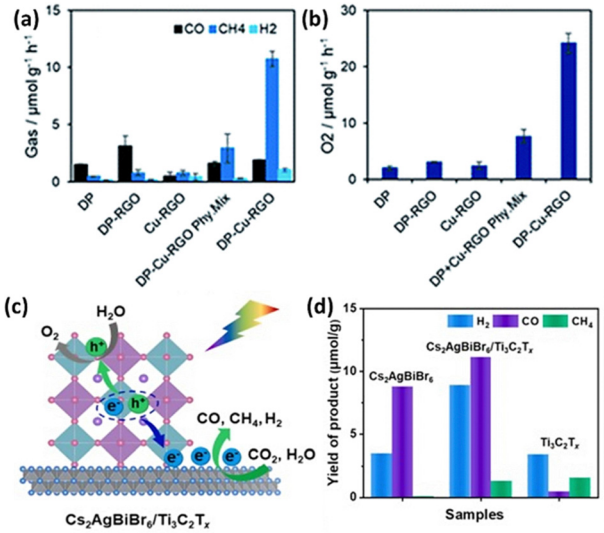

Fig. 8 (a) Production rates of CO, CH_4, H_2, and (b) O_2 from the photocatalytic reduction of CO_2 using water vapor as a proton source on various photocatalysts under simulated solar light for 4 hours.[104] Reproduced with permission from ref. 104 Copyright © 2022 Wiley-VCH GmbH. (c) Diagram illustrating the mechanism of photocatalytic CO_2 reduction by $Cs_2AgBiBr_6/Ti_3C_2T_x$ heterostructures under visible light irradiation. (d) Comparison of the photocatalytic activity between $Cs_2AgBiBr_6$, $Ti_3C_2T_x$, and $Cs_2AgBiBr_6/Ti_3C_2T_x$ heterostructures for CO_2 reduction.[110] Reproduced with permission from ref. 110 Copyright © 2022 Elsevier B.V. All rights reserved.

separating photoinduced charge carriers, enabling two semiconductors to simultaneously harness solar energy.[111] When light is incident upon them, electrons generated in the conduction band of the oxidative semiconductor are transferred to the valence band of the reductive semiconductor, where they recombine.[112]

Mahmoud *et al.* proposed a Z-scheme heterostructure involving $Cs_2AgBiBr_6$ (CABB) and Sr_2FeNbO_6 (SFNO).[113] The energy band gaps of CABB and SFNO were determined to be 2.17 eV and 2.04 eV, respectively, with conduction band minima (CBM) located at −0.57 V and 0.10 V (relative to the NHE at pH = 7), as depicted in Fig. 9(a). This configuration facilitates the efficient transfer of electrons from SFNO's CBM to CABB's VBM when exposed to light. As observed in the time-resolved PL decay shown in Fig. 9(b), this heterostructure promotes effective spatial charge separation. The CABB/SFNO Z-scheme photocatalyst exhibited remarkable CO and CH_4 production rates of 50.00 and 8.12 μmol g^{-1} h^{-1}, respectively, as illustrated in Fig. 9(c). This enhanced performance is attributed to the unique Z-scheme heterojunction, which effectively separates charge carriers in space. Research utilizing the Z-scheme approach is gaining attention due to its simplicity in synthesizing heterostructures. Wu *et al.* used a simple hot injection method to grow CABB nanocrystals *in situ* on the surface of Bi_2WO_6 (BWO) nanosheets.[114] As shown in Fig. 9(d), the resulting CABB/BWO heterojunction, thanks to the presence of spatial charge separation characteristic of a Z-scheme, exhibited high photocatalytic activity with a substantial electron consumption rate of 87.66 μmol g^{-1} h^{-1} under simulated sunlight conditions (AM 1.5G).

Continuing research endeavors involve the integration of 2D materials with perovskites within Z-scheme systems to enhance CO_2 reduction performance. For example, the 2D organic semiconductor g-C_3N_4, which previously exhibited unsatisfactory photocatalytic activity for CO_2 reduction due to rapid carrier recombination and inefficient utilization of visible light,[115] has been combined with CABB in a Z-scheme configuration.[116] This innovative combination capitalizes on g-C3N4's CBM reduction ability and CABB's VBM oxidation capability, resulting in impressive CH_4 production with high selectivity. Furthermore, research by Li *et al.* has elucidated the Z-scheme photocatalytic mechanism of $SnS/(CH_3NH_3)_2AgBiI_6$, analyzing band energy positions and interfacial charge transfer.[117] The interaction at the interface between the $(CH_3NH_3)_2AgBiI_6$ (010) surface and SnS monolayers induces electron flow from SnS to the $(CH_3NH_3)_2AgBiI_6$ (010) surface. As seen in Fig. 9(e) and (f), Calculations of Gibbs free energy changes (ΔG) in comparison between the $(CH_3NH_3)_2AgBiI_6$ surface and $SnS/(CH_3NH_3)_2AgBiI_6$ revealed a decrease from 2.17 to 1.72 eV. This outcome signifies that $SnS/(CH_3NH_3)_2AgBiI_6$ enhances the photocatalytic activity for CO_2 reduction.

6. Summary and prospects

LFDHP has garnered significant attention in the fields of photocatalytic hydrogen production and CO_2 reduction due to its exceptional optical properties, adjustable bandgap, superior charge carrier transport capabilities, and abundant active sites. This review provides an overview of LFDHP, its synthesis methods, and recent research on its applications in hydrogen production and CO_2 reduction over the past few years. It was summarized in Fig. 10. It serves as a valuable reference for the development of new LFDHP photocatalysts with high efficiency and selectivity for hydrogen production and CO_2 conversion. While LFDHP photocatalysts for hydrogen production and CO_2 reduction have achieved many successes in recent years, there is still much room for improvement, which can be summarized in terms of material aspects, hydrogen production catalysis, CO_2 reduction catalysis, and theoretical considerations.

6.1. Material aspects

Currently, LFDHP photocatalysts primarily focus on the BiAg-based perovskite structure type. These photocatalysts possess an appropriate bandgap and band structure but suffer from unsatisfactory performance due to undesired electron–hole recombination. To address this issue, it is possible to adjust the electron band structure through doping or substituting elements, thereby enhancing visible light utilization efficiency and oxidative reduction capacity. Another approach to suppress carrier recombination in bulk photocatalysts is by reducing the size of perovskite powder to nanocrystals or quantum dots. Heterojunction photocatalysts offer a method to improve the spatial separation of photogenerated charge carriers, resulting

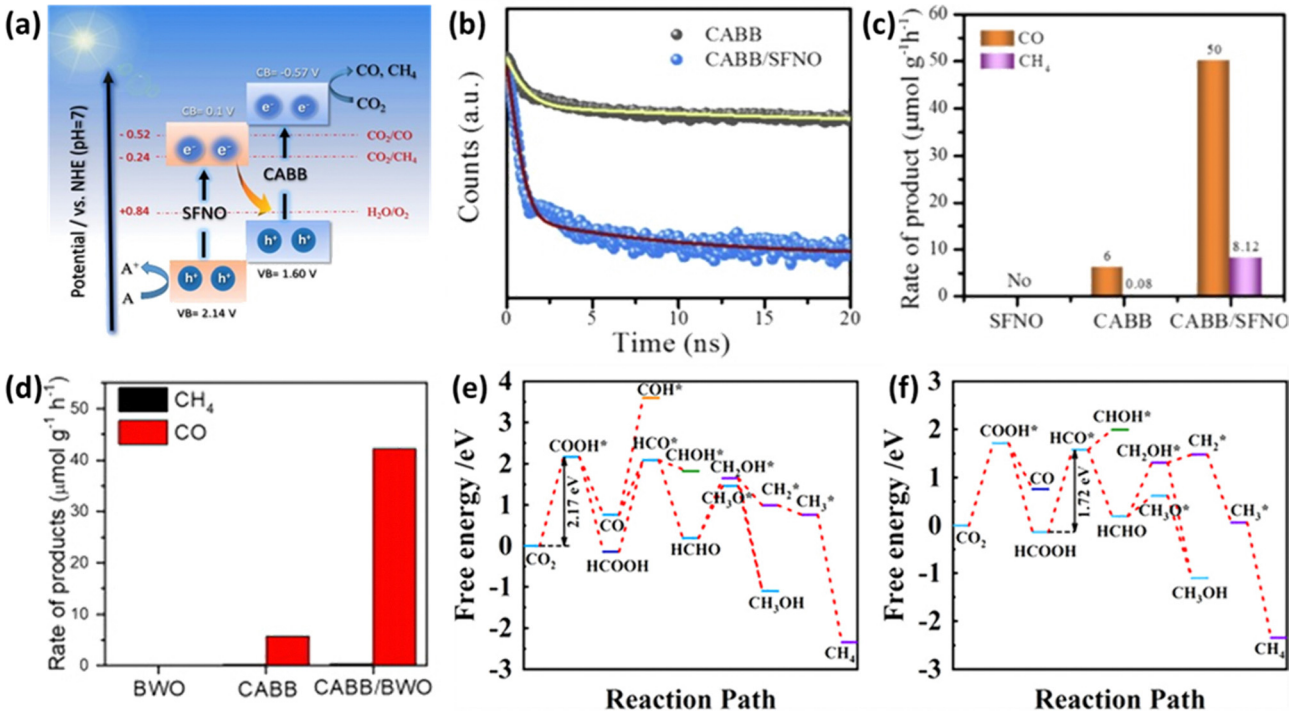

Fig. 9 (a) Illustration of the potential reaction mechanism of the CABB/SFNO Z-scheme heterojunction. (b) Steady-state PL (photoluminescence) and TRPL (Time-Resolved Photoluminescence) decay spectra of CABB and CABB/SFNO heterojunction. (c) Photocatalytic activity test comparing SFNO, CABB, and CABB/SFNO heterojunction.[113] Reproduced with permission from ref. 113 Copyright © 2022 Elsevier B.V. All rights reserved. (d) Photocatalytic activity test comparing CABB, BWO, and CABB/BWO.[114] Reproduced with permission from ref. 114 Copyright © 2022 Elsevier Inc. All rights reserved. (e) Free energy diagram depicting possible reaction pathways for CO_2 reduction on the $(CH_3NH_3)_2AgBiI_6$ (010) surface. (f) Free energy diagram illustrating possible reaction pathways for CO_2 reduction on the $SnS/(CH_3NH_3)_2AgBiI_6$ heterostructure.[117] Reproduced with permission from ref. 117 Copyright Copyright © 2022, American Chemical Society.

in high-efficiency photocatalytic performance. Loading cocatalysts can inhibit charge carrier recombination and increase active sites, further improving photocatalytic activity.

6.2. Aspects of hydrogen production photocatalysis

Due to LFDHP's sensitivity to moisture, conducting photocatalytic reactions in halogen acid solutions has proven effective for hydrogen generation. However, it's essential to note that this does not imply complete safety of LFDHP in halogen acids. Thus, researching excellent sealing techniques to restrict contact between LFDHP and polar solvents is crucial. The sealing material must be transparent enough to ensure sufficient light absorption by LFDHP and possess excellent conductivity for effective carrier extraction. Commonly used sealing materials include transparent resins (epoxy) and conductive carbon paste. Some studies encapsulate LFDHP within a Photovoltaic-photoelectrochemical cell (PV-PEC) to protect perovskite from polar solvents. This system gains attention as it increases the oxidation–reduction capacity of the PEC cell, enabling higher voltages in series due to the presence of solar components. Additionally, research on LFDHP with excellent water stability for direct hydrogen production in water is gradually increasing. Alongside improving water stability, researching LFDHP with high photocatalytic activity will be a crucial breakthrough in future studies.

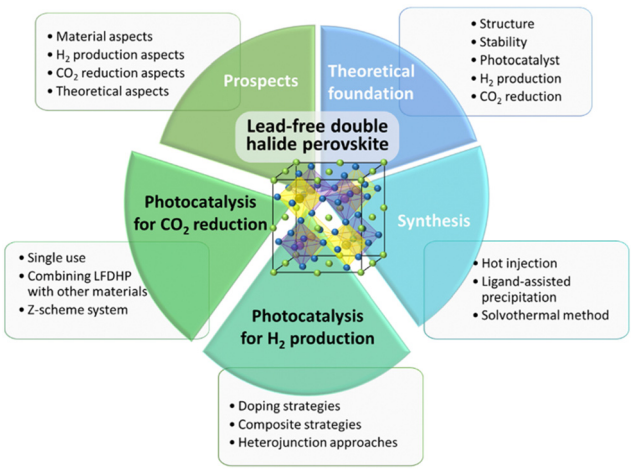

Fig. 10 Visual overview of review content.

6.3. Aspects of CO_2 reduction

Research on the stability of LFDHP for photocatalytic CO_2 reduction, charge carrier mobility, electron–hole recombination, and catalyst activity mechanisms is essential. Furthermore, studying the impact of photon energy, irradiation time, catalytic reaction, reaction medium, and O_2 production on LFDHP's

stability and photocatalytic performance is necessary. Doping is one method to enhance the CO_2 reduction performance of photocatalysts by partially replacing some atoms in the perovskite composition. This approach allows for bandgap adjustment to increase light absorption efficiency and control the CBM. Heterojunctions with superior optical properties, such as 2D semiconductors, can facilitate the separation of photogenerated electron–hole pairs. Another effective approach is immobilizing metal nanoparticles on the surface of LFDHP, forming Schottky heterojunctions.

6.4. Theoretical aspects

To provide guidelines for improving photocatalytic efficiency, detailed information about the photocatalytic process, especially the reaction pathways and kinetics of photogenerated charge carriers in perovskite materials, is needed. Therefore, a comprehensive theoretical model is essential to interpret the role of perovskite materials in photocatalytic oxidation–reduction reactions. Theoretical approaches like Density Functional Theory (DFT) can help understand existing research and provide guidance for developing more efficient photocatalysts for oxidation–reduction reactions. In addition to theoretical calculations, on-site characterization techniques can support mechanism studies.[118] For example, *in situ* X-ray photoelectron spectroscopy (XPS) can investigate electron transfer pathways by observing changes in binding energy. *In situ* X-ray absorption spectroscopy (XAS) can study the evolution of electronic structure on the catalyst's surface and monitor dynamic changes in the state of metal atoms, identifying active sites. Time-resolved ultrafast spectroscopy can provide a comprehensive and reliable understanding of charge carrier behaviour in LFDHP. Continued exploration in these promising areas is expected to lead to significant improvements in the efficiency and stability of LFDHP hydrogen production and CO_2 reduction photocatalysts, making practical applications possible in the near future.

Conflicts of interest

There are no conflicts to declare.

Acknowledgements

This research was supported by the National Research Foundation of Korea (NRF) (2022M3H4A1A01012712, 2022M3H4A1A04096380).

Notes and references

1 Global temperature trend monitor, https://cds.climate.copernicus.eu/cdsapp#!/software/app-c3s-global-temperature-trend-monitor?tab=app, (accessed 11 July 2023).
2 J. Luo, W. Zhang, H. Yang, Q. Fan, F. Xiong, S. Liu, D. S. Li and B. Liu, *EcoMat*, 2021, **3**, e12079.
3 A. Fujishima and K. Honda, *Nature*, 1972, **238**, 37–38.
4 L. Wang, J. Zhang, Y. Zhang, H. Yu, Y. Qu and J. Yu, *Small*, 2022, **18**, 2104561.
5 W. Jiang, H. Loh, B. Q. L. Low, H. Zhu, J. Low, J. Z. X. Heng, K. Y. Tang, Z. Li, X. J. Loh, E. Ye and Y. Xiong, *Appl. Catal., B*, 2023, **321**, 122079.
6 C. Karthikeyan, P. Arunachalam, K. Ramachandran, A. M. Al-Mayouf and S. Karuppuchamy, *J. Alloys Compd.*, 2020, **828**, 154281.
7 H. H. Do, D. L. T. Nguyen, X. C. Nguyen, T. H. Le, T. P. Nguyen, Q. T. Trinh, S. H. Ahn, D. V. N. Vo, S. Y. Kim and Q. V. Le, *Arabian J. Chem.*, 2020, **13**(2), 3653–3671.
8 T. P. Nguyen, D. L. T. Nguyen, V. H. Nguyen, T. H. Le, D. V. N. Vo, Q. T. Trinh, S. R. Bae, S. Y. Chae, S. Y. Kim and Q. Van Le, *Nanomaterials*, 2020, 10.
9 Z. Cheng, W. Qi, C. Heng Pang, T. Thomas, T. Wu, S. Liu, M. Yang, Z. Cheng, W. Qi, S. Liu, M. Yang, C. H. Pang, T. Wu and T. Thomas, *Adv. Funct. Mater.*, 2021, **31**, 2100553.
10 H. S. Gujral, G. Singh, A. V. Baskar, X. Guan, X. Geng, A. V. Kotkondawar, S. Rayalu, P. Kumar, A. Karakoti and A. Vinu, *Sci. Technol. Adv. Mater.*, 2022, **23**, 76–119.
11 S. L. Lee and C.-J. Chang, *Catalysts*, 2019, **9**, 457.
12 S. Zhang, X. Ou, Q. Xiang, S. Carabineiro, J. Fan and K. Lv, *Chemosphere*, 2022, **303**, 135085.
13 Q. Zhu, Q. Xu, M. Du, X. Zeng, G. Zhong, B. Qiu, J. Zhang, Q. H. Zhu, Q. Xu, X. F. Zeng, G. F. Zhong, M. M. Du, B. C. Qiu and J. L. Zhang, *Adv. Mater.*, 2022, **34**, 2202929.
14 S. Tasleem, M. Tahir and W. A. Khalifa, *Int. J. Hydrogen Energy*, 2021, **46**, 14148–14189.
15 S. Gautam, H. Agrawal, M. Thakur, A. Akbari, H. Sharda, R. Kaur and M. Amini, *J. Environ. Chem. Eng.*, 2020, **8**, 103726.
16 J. Chen, R. Abazari, K. A. Adegoke, N. W. Maxakato, O. S. Bello, M. Tahir, S. Tasleem, S. Sanati, A. M. Kirillov and Y. Zhou, *Coord. Chem. Rev.*, 2022, **469**, 214664.
17 S. A. Younis, E. E. Kwon, M. Qasim, K. H. Kim, T. Kim, D. Kukkar, X. Dou and I. Ali, *Prog. Energy Combust. Sci.*, 2020, **81**, 100870.
18 J. You, Y. Zhao, L. Wang and W. Bao, *J. Cleaner Prod.*, 2021, **291**, 125822.
19 H. Wang, H. Wang, Z. Wang, L. Tang, G. Zeng, P. Xu, M. Chen, T. Xiong, C. Zhou, X. Li, D. Huang, Y. Zhu, Z. Wang and J. Tang, *Chem. Soc. Rev.*, 2020, **49**, 4135–4165.
20 Y. Zhou, F. Lu, T. Fang, D. Gu, X. Feng, T. Song and W. Liu, *J. Alloys Compd.*, 2022, **911**, 165062.
21 Y. Tang, C. H. Mak, G. Jia, K. C. Cheng, J. J. Kai, C. W. Hsieh, F. Meng, W. Niu, F. F. Li, H. H. Shen, X. Zhu, H. M. Chen and H. Y. Hsu, *J. Mater. Chem. A*, 2022, **10**, 12296–12316.
22 V. H. Nguyen, B. S. Nguyen, Z. Jin, M. Shokouhimehr, H. W. Jang, C. Hu, P. Singh, P. Raizada, W. Peng, S. Shiung Lam, C. Xia, C. C. Nguyen, S. Y. Kim and Q. Van Le, *Chem. Eng. J.*, 2020, 402.
23 B. M. Bresolin, Y. Park and D. W. Bahnemann, *Catalysts*, 2020, **10**, 709.
24 X. Qian, Z. Chen, X. Yang, W. Zhao, C. Liu, T. Sun, D. Zhou, Q. Yang, G. Wei and M. Fan, *J. Cleaner Prod.*, 2020, **249**, 119335.

25 D. Y. Heo, T. H. Lee, A. Iwan, L. Kavan, M. Omatova, E. Majkova, K. Kamarás, H. W. Jang and S. Y. Kim, *J. Power Sources*, 2020, **458**, 228067.
26 E. Aktas, N. Rajamanickam, J. Pascual, S. Hu, M. H. Aldamasy, D. Di Girolamo, W. Li, G. Nasti, E. Martínez-Ferrero, A. Wakamiya, E. Palomares and A. Abate, *Commun. Mater.*, 2022, **3**, 1–14.
27 P. K. Kung, M. H. Li, P. Y. Lin, J. Y. Jhang, M. Pantaler, D. C. Lupascu, G. Grancini and P. Chen, *Solar RRL*, 2020, **4**, 1900306.
28 W. Cao, Z. Hu, Z. Lin, X. Guo, J. Su, J. Chang and Y. Hao, *J. Energy Chem.*, 2022, **68**, 420–438.
29 M. Ikram, R. Malik, R. Raees, M. Imran, F. Wang, S. Ali, M. Khan, Q. Khan and M. Maqbool, *Sustain. Energy Technol. Assess.*, 2022, **53**, 102433.
30 E. Aktas, N. Rajamanickam, J. Pascual, S. Hu, M. H. Aldamasy, D. Di Girolamo, W. Li, G. Nasti, E. Martínez-Ferrero, A. Wakamiya, E. Palomares and A. Abate, *Commun. Mater.*, 2022, **3**, 1–14.
31 J. Lu, C. Yan, W. Feng, X. Guan, K. Lin and Z. Wei, *EcoMat*, 2021, **3**, e12082.
32 S. Z. Wang, J. T. Wang, Y. H. Lou, Y. H. Zhou and Z. K. Wang, *Adv. Mater. Interfaces*, 2022, **9**, 2200772.
33 M. J. Seol, J. W. Han, S. H. Hwang and S. Y. Kim, *J. Korean Institute Metals Mater.*, 2022, 60.
34 Y.-T. Huang, S. R. Kavanagh, D. O. Scanlon, G. Kaur, A. Shukla, K. Justice Babu, M. Nath Tripathi, A. Saha, S. Singh, J. Ghosh, P. J. Sellin and P. K. Giri, *Nanotechnology*, 2022, **33**, 312001.
35 T. Jiang, W. Ma, H. Zhang, Y. Tian, G. Lin, W. Xiao, X. Yu, J. Qiu, X. Xu, Y. Yang, D. Ju, T. Jiang, W. Ma, Y. Tian, W. Xiao, Y. Yang, H. Zhang, X. Yu, J. Qiu, X. Xu, G. Lin and D. Ju, *Adv. Funct. Mater.*, 2021, **31**, 2009973.
36 G. S. H. Thien, M. Ab Rahman, B. K. Yap, N. M. L. Tan, Z. He, P. L. Low, N. K. Devaraj, A. F. Ahmad Osman, Y. K. Sin and K. Y. Chan, *ACS Omega*, 2022, **7**, 39472–39481.
37 Y. Fang, S. Zhai, L. Chu and J. Zhong, *ACS Appl. Mater. Interfaces*, 2021, **13**, 17141–17157.
38 W. J. Jang, H. W. Jang and S. Y. Kim, *Small Methods*, 2023, 2300207.
39 U. Farooq, M. Ishaq, U. A. Shah, S. Chen, Z. H. Zheng, M. Azam, Z. H. Su, R. Tang, P. Fan, Y. Bai and G. X. Liang, *Nano Energy*, 2022, **92**, 106710.
40 I. Dincer and C. Zamfirescu, *Sustainable Hydrogen Production*, 2016, pp. 309–391.
41 C. Acar, I. Dincer and C. Zamfirescu, *Int. J. Energy Res.*, 2014, **38**, 1903–1920.
42 P. Zhang, J. Yang and S. H. Wei, *J. Mater. Chem. A*, 2018, **6**(4), 1809–1815.
43 F. Igbari, Z. K. Wang and L. S. Liao, *Adv. Energy Mater.*, 2019, **9**, 1803150.
44 F. Giustino and H. J. Snaith, *ACS Energy Lett.*, 2016, **1**, 1233–1240.
45 G. Li, K. Chen, Y. Cui, Y. Zhang, Y. Tian, B. Tian, Y. Hao, Y. Wu and H. Zhang, *Adv. Opt. Mater.*, 2020, **8**, 1902012.
46 W. Travis, E. N. K. Glover, H. Bronstein, D. O. Scanlon and R. G. Palgrave, *Chem. Sci.*, 2016, **7**, 4548–4556.
47 K. Vighnesh, S. Wang, H. Liu and A. L. Rogach, *ACS Nano*, 2022, **16**, 19618–19625.
48 D. Zhu, J. Zito, V. Pinchetti, Z. Dang, A. Olivati, L. Pasquale, A. Tang, M. L. Zaffalon, F. Meinardi, I. Infante, L. De Trizio, L. Manna and S. Brovelli, *ACS Energy Lett.*, 2020, **5**, 1840–1847.
49 M. Liu, S. K. Matta, H. Ali-Löytty, A. Matuhina, G. K. Grandhi, K. Lahtonen, S. P. Russo and P. Vivo, *Nano Lett.*, 2022, **22**, 311–318.
50 F. Zhang, H. Zhong, C. Chen, X. G. Wu, X. Hu, H. Huang, J. Han, B. Zou and Y. Dong, *ACS Nano*, 2015, **9**, 4533–4542.
51 Y. T. Yoo, D. Y. Heo, S. R. Bae, J. Park, T. W. Lee, H. W. Jang, S. H. Ahn and S. Y. Kim, *Small Methods*, 2021, **5**, 2100054.
52 Y. Guo, Y. Lou, J. Chen and Y. Zhao, *ChemSusChem*, 2022, **15**, e202102334.
53 D. Chen, G. Fang, X. Chen, L. Lei, J. Zhong, Q. Mao, S. Zhou and J. Li, *J. Mater. Chem. C*, 2018, **6**, 8990–8998.
54 D. Chen, G. Fang, X. Chen, L. Lei, J. Zhong, Q. Mao, S. Zhou and J. Li, *J. Mater. Chem. C*, 2018, **6**, 8990–8998.
55 Y. J. Low, J. Y. C. Liew, M. A. Kamarudin, H. N. Lim, F. D. Muhammad, K. P. Lim, M. H. M. Zaid, T. F. Choo, H. K. Lee, Y. W. Fen, S. Hayase and Z. A. Talib, *Mater. Today Chem.*, 2023, **29**, 101477.
56 A. H. Slavney, T. Hu, A. M. Lindenberg and H. I. Karunadasa, *J. Am. Chem. Soc.*, 2016, **138**, 2138–2141.
57 H. Dong, C. Ran, W. Gao, N. Sun, X. Liu, Y. Xia, Y. Chen and W. Huang, *Adv. Energy Mater.*, 2022, **12**, 2102213.
58 A. Aftab and M. I. Ahmad, *Sol. Energy*, 2021, **216**, 26–47.
59 R. Chiara, M. Morana and L. Malavasi, *ChemPlusChem*, 2021, **86**, 879–888.
60 D. Y. Heo, T. H. Lee, A. Iwan, L. Kavan, M. Omatova, E. Majkova, K. Kamarás, H. W. Jang and S. Y. Kim, *J. Power Sources*, 2020, **458**, 228067.
61 A. Yadegarifard, H. Lee, H. J. Seok, I. Kim, B. K. Ju, H. K. Kim and D. K. Lee, *Nano Energy*, 2023, **112**, 108481.
62 F. Yang, D. Hirotani, G. Kapil, M. A. Kamarudin, C. H. Ng, Y. Zhang, I. Shen, S. Hayase and Y. H. Zhang, *Angew. Chem.*, 2018, **130**, 12927–12931.
63 X. G. Zhao, J. H. Yang, Y. Fu, D. Yang, Q. Xu, L. Yu, S. H. Wei and L. Zhang, *J. Am. Chem. Soc.*, 2017, **139**, 2630–2638.
64 S. Chand Yadav, A. Srivastava, V. Manjunath, A. Kanwade, R. S. Devan and P. M. Shirage, *Mater. Today Phys.*, 2022, **26**, 100731.
65 P. Barbier, M. Drache, G. Mairesse and J. Ravez, *J. Solid State Chem.*, 1982, **42**, 130–135.
66 W. Urland, *Chem. Phys. Lett.*, 1981, **83**, 116–119.
67 E. T. McClure, M. R. Ball, W. Windl and P. M. Woodward, *Chem. Mater.*, 2016, **28**, 1348–1354.
68 A. H. Slavney, T. Hu, A. M. Lindenberg and H. I. Karunadasa, *J. Am. Chem. Soc.*, 2016, **138**, 2138–2141.
69 M. Shirayama, M. Kato, T. Miyadera, T. Sugita, T. Fujiseki, S. Hara, H. Kadowaki, D. Murata, M. Chikamatsu and H. Fujiwara, *J. Appl. Phys.*, 2016, **119**, 115501.
70 L. Z. Lei, Z. F. Shi, Y. Li, Z. Z. Ma, F. Zhang, T. T. Xu, Y. T. Tian, D. Wu, X. J. Li and G. T. Du, *J. Mater. Chem. C*, 2018, **6**, 7982–7988.
71 J. Lao, W. Xu, C. Jiang, N. Zhong, B. Tian, H. Lin, C. Luo, J. Travas-Sejdic, H. Peng and C. G. Duan, *J. Mater. Chem. C*, 2021, **9**, 5706–5712.

72 J. Zhou, Z. Xia, M. S. Molokeev, X. Zhang, D. Peng and Q. Liu, *J. Mater. Chem. A*, 2017, **5**, 15031–15037.
73 K. Li, S. Li, W. Zhang, Z. Shi, D. Wu, X. Chen, P. Lin, Y. Tian and X. Li, *J. Colloid Interface Sci.*, 2021, **596**, 376–383.
74 J. Wang, S. Yip, S. R. Phillpot and D. Wolf, *Phys. Rev. Lett.*, 1993, **71**, 4182–4185.
75 K. Radja, B. L. Farah, A. Ibrahim, D. Lamia, I. Fatima, B. Nabil, A. Mohamed, Y. Al-Douri and A. F. A. El-Rehim, *J. Phys. Chem. Solids*, 2022, **167**, 110795.
76 M. A. Ghebouli, T. Chihi, B. Ghebouli and M. Fatmi, *Chin. J. Phys.*, 2018, **56**, 323–330.
77 6.4 The Solar Spectrum | METEO 300: Fundamentals of Atmospheric Science, **https://www.e-education.psu.edu/meteo300/node/683**, (accessed 23 August 2023).
78 Y. Dai and Y. Xiong, *Nano Res. Energy*, 2022, **1**, e9120006.
79 Z. Wu, H. Tüysüz, F. Besenbacher, Y. Dai and Y. Xiong, *Nanoscale*, 2023, **15**, 5598–5622.
80 C. Acar, I. Dincer and G. F. Naterer, *Int. J. Energy Res.*, 2016, **40**, 1449–1473.
81 I. Dincer and C. Acar, *Int. J. Hydrogen Energy*, 2015, **40**, 11094–11111.
82 F. Qi, Y. Pu, D. Wu, X. Tang and Q. Huang, *Chemical Record*, 2023, e202300078.
83 G. H. Han, J. Bang, G. Park, S. Choe, Y. J. Jang, H. W. Jang, S. Y. Kim and S. H. Ahn, *Small*, 2023, **19**, 2205765.
84 E. Gong, S. Ali, C. B. Hiragond, H. S. Kim, N. S. Powar, D. Kim, H. Kim and S. Il In, *Energy Environ. Sci.*, 2022, **15**, 880–937.
85 M. Shi, G. Li, W. Tian, S. Jin, X. Tao, Y. Jiang, E. A. Pidko, R. Li, C. Li, M. Shi, X. Tao, Y. Jiang, R. Li, C. Li, G. Li, E. A. Pidko, W. Tian and S. Jin, *Adv. Mater.*, 2020, **32**, 2002137.
86 G. Chen, P. Wang, Y. Wu, Q. Zhang, Q. Wu, Z. Wang, Z. Zheng, Y. Liu, Y. Dai, B. G. Huang Chen, P. Wang, Y. Wu, Q. Zhang, Z. Wang, Z. Zheng, Y. Liu, B. Huang, Q. Wu and Y. Dai, *Adv. Mater.*, 2020, **32**, 2001344.
87 A. H. Slavney, L. Leppert, D. Bartesaghi, A. Gold-Parker, M. F. Toney, T. J. Savenije, J. B. Neaton and H. I. Karunadasa, *J. Am. Chem. Soc.*, 2017, **139**, 5015–5018.
88 J. Shang, W. Hao, X. Lv, T. Wang, X. Wang, Y. Du, S. Dou, T. Xie, D. Wang and J. Wang, *ACS Catal.*, 2014, **4**, 954–961.
89 Z. He, Q. Tang, X. Liu, X. Yan, K. Li and D. Yue, *Energy Fuels*, 2021, **35**, 15005–15009.
90 T. Wang, D. Yue, X. Li and Y. Zhao, *Appl. Catal., B*, 2020, **268**, 118399.
91 Y. Jiang, K. Li, X. Wu, M. Zhu, H. Zhang, K. Zhang, Y. Wang, K. P. Loh, Y. Shi and Q. H. Xu, *ACS Appl. Mater. Interfaces*, 2021, **13**, 10037–10046.
92 X. Li, X. Lv, N. Li, J. Wu, Y. Z. Zheng and X. Tao, *Appl. Catal., B*, 2019, **243**, 76–85.
93 Y. Zhang, Z. Sun, Z. Wang, Y. Zang and X. Tao, *Int. J. Hydrogen Energy*, 2022, **47**, 8829–8840.
94 Q. Huang, Y. Guo, J. Chen, Y. Lou and Y. Zhao, *New J. Chem.*, 2022, **46**, 7395–7402.
95 Q. Xu, L. Zhang, B. Cheng, J. Fan and J. Yu, *Chem*, 2020, 6.
96 L. Zhou, Y. Li, S. Yang, M. Zhang, Z. Wu, R. Jin and Y. Xing, *Chem. Eng. J.*, 2021, **420**, 130361.
97 F. Xu, K. Meng, B. Cheng, S. Wang, J. Xu and J. Yu, *Nat. Commun.*, 2020, **11**, 4613.
98 H. Lv, H. Yin, N. Jiao, C. Yuan, S. Weng, K. Zhou, Y. Dang, X. Wang, Z. Lu and Y. Zhang, *Small Methods*, 2023, **7**, 2201365.
99 L. Zhou, Y. F. Xu, B. X. Chen, D. Bin Kuang and C. Y. Su, *Small*, 2018, **14**, 1703762.
100 Z. Liu, H. Yang, J. Wang, Y. Yuan, K. Hills-Kimball, T. Cai, P. Wang, A. Tang and O. Chen, *Nano Lett.*, 2021, **21**, 1620–1627.
101 J. Ran, M. Jaroniec and S. Z. Qiao, *Adv. Mater.*, 2018, 30.
102 J. Pi, X. Jia, Z. Long, S. Yang, H. Wu, D. Zhou, Q. Wang, H. Zheng, Y. Yang, J. Zhang and J. Qiu, *Adv. Energy Mater.*, 2022, **12**, 2202074.
103 T. Chen, M. Zhou, W. Chen, Y. Zhang, S. Ou and Y. Liu, *Sustain Energy Fuels*, 2021, **5**, 3598–3605.
104 S. Kumar, I. Hassan, M. Regue, S. Gonzalez-Carrero, E. Rattner, M. A. Isaacs and S. Eslava, *J. Mater. Chem. A*, 2021, **9**, 12179–12187.
105 F. Yang, A. O. Elnabawy, R. Schimmenti, P. Song, J. Wang, Z. Peng, S. Yao, R. Deng, S. Song, Y. Lin, M. Mavrikakis and W. Xu, *Nat. Commun.*, 2020, **11**, 1088.
106 J. Cui, M. Daboczi, M. Regue, Y. C. Chin, K. Pagano, J. Zhang, M. A. Isaacs, G. Kerherve, A. Mornto, J. West, S. Gimenez, J. S. Kim and S. Eslava, *Adv. Funct. Mater.*, 2022, **32**, 2207136.
107 M. S. Sena, J. Cui, Y. Baghdadi, E. Rattner, M. Daboczi, A. L. Lopes-Moriyama, A. G. dos Santos and S. Eslava, *ACS Appl. Energy Mater.*, 2023, **6**(20), 10193–10204.
108 B. Anasori, M. R. Lukatskaya and Y. Gogotsi, *Nat. Rev. Mater.*, 2017, 2.
109 G. Eda and S. A. Maier, *ACS Nano*, 2013, 7.
110 Z. Zhang, B. Wang, H. B. Zhao, J. F. Liao, Z. C. Zhou, T. Liu, B. He, Q. Wei, S. Chen, H. Y. Chen, D. Bin Kuang, Y. Li and G. Xing, *Appl. Catal., B*, 2022, **312**, 121358.
111 M. Ebihara, T. Ikeda, S. Okunaka, H. Tokudome, K. Domen and K. Katayama, *Nat. Commun.*, 2021, **12**, 3716.
112 P. Zhou, J. Yu and M. Jaroniec, *Adv. Mater.* 2014, 26.
113 A. Mahmoud Idris, S. Zheng, L. Wu, S. Zhou, H. Lin, Z. Chen, L. Xu, J. Wang and Z. Li, *Chem. Eng. J.*, 2022, **446**, 137197.
114 L. Wu, S. Zheng, H. Lin, S. Zhou, A. Mahmoud Idris, J. Wang, S. Li and Z. Li, *J. Colloid Interface Sci.*, 2023, **629**, 233–242.
115 Y. Ren, D. Zeng and W. J. Ong, *Cuihua Xuebao*, 2019, **40**, 289–319.
116 Y. Wang, H. Huang, Z. Zhang, C. Wang, Y. Yang, Q. Li and D. Xu, *Appl. Catal., B*, 2021, **282**, 119570.
117 P. Li, Y. Lin, M. Ma, M. Zhang, J. Li, Z. Wang, V. Maheskumar, Z. Y. Jiang and R. Zhang, *ACS Appl. Energy Mater.*, 2022, **5**, 1942–1952.
118 X. Wang, B. Hu, Y. Li and G. Zhang, *Solar RRL*, 2023, **7**(18), 2300410.